



Society of Petroleum Engineers

**SPE-189901-MS**

## **Interaction Between Hydraulic Fracture and a Preexisting Fracture under Triaxial Stress Conditions**

Saied Mighani<sup>1</sup>, David A. Lockner<sup>2</sup>, Brian D. Kilgore<sup>2</sup>, Farrokh Sheibani<sup>1</sup> and Brian Evans<sup>1</sup>

<sup>1</sup>Department of Earth Atmospheric and Planetary Sciences, Massachusetts Institute of Technology, Cambridge, Massachusetts, USA <sup>2</sup>U.S. Geological Survey, Menlo Park, California, USA

Copyright 2018, Society of Petroleum Engineers

This paper was prepared for presentation at the SPE Hydraulic Fracturing Technology Conference held in The Woodlands, TX, USA, 23-25 January 2018.

This paper was selected for presentation by an SPE program committee following review of information contained in an abstract submitted by the author(s). Contents of the paper have not been reviewed by the Society of Petroleum Engineers and are subject to correction by the author(s). The material does not necessarily reflect any position of the Society of Petroleum Engineers, its officers, or members. Electronic reproduction, distribution, or storage of any part of this paper without the written consent of the Society of Petroleum Engineers is prohibited. Permission to reproduce in print is restricted to an abstract of not more than 300 words; illustrations may not be copied. The abstract must contain conspicuous acknowledgment of SPE copyright.

---

### **Abstract**

Enhanced reservoir connectivity generally requires maximizing the intersection between hydraulic fracture (HF) and preexisting underground natural fractures (NF), while having the hydraulic fracture cross the natural fractures (and not arrest). We have studied the interaction between a hydraulic fracture and a polished saw-cut fault. The experiments include a hydraulic fracture initiating from a pressurized axial borehole (using water) that approaches a dry fault that is inclined at an angle  $\theta$  with respect to the borehole axis. The experiments are conducted on Poly(methyl) Meta Acrylate (PMMA) and Solnhofen limestone, a finely grained ( $<5 \mu\text{m}$  grain), low permeability ( $<10 \text{ nD}$ ) carbonate. The confining pressure in all experiments is 5 MPa, while the differential stress (1-80 MPa) and approach angle,  $\theta$  (30, 45, 60, 90°) are experimental variables. During the hydraulic fracture, acoustic emissions (AE), slip velocity, slip magnitude, stress drop and pore pressure are recorded at a 5 MHz sampling rate. A Doppler laser vibrometer measures piston velocity outside the pressure vessel to infer fault slip duration and a strain gage adjacent to the saw-cut provides a near-field measure of axial stress.

For PMMA, the coefficient of friction was 0.30 and sliding was unstable (stick-slip). The approaching HF in PMMA created a tensile fracture detected by AE transducers  $\sim 100 \mu\text{s}$  before the significant stick-slip event (45% stress drop and slip velocity of  $\sim 60 \text{ mm/s}$ ) and was arrested by the fault at all fault orientations and differential stresses, even at 90° fault orientation and 80 MPa differential stress. For Solnhofen limestone, we observed stable sliding at a coefficient of friction of 0.12. In contrast to PMMA, the HF in Solnhofen consistently crossed to the other side of the fault. When the HF crossed the fault, it produced a small stress drop ( $<10\%$ ) and slip velocity of only 0.5 mm/s. Theoretical models by Blanton (1986) and Renshaw and Pollard (1995) predict that HF will be arrested for Solnhofen limestone and cross PMMA 90° fault at 80 MPa differential stress. Although the exact cause for the discrepancy between experiments and the theory is not known, one feature present in the experiments but not considered in the models, is the diffusion of fluid driven by the fault slip. Thus, the formation of a “fluid-filled patch” on the fault surface as it is intersected by the HF may substantially impact the crossing/arrest behavior. The approach angle and differential stress also influence the HF initiation azimuth and breakdown pressure. In most cases, the HF initiation azimuth was normal to the fault strike. These observations suggest that the presence of natural fractures could result in rotation of hydraulic fractures to be more normal to their strike and a subsequent change in the downhole pressure recordings. The latter could be used as a diagnostic tool for predicting this interaction.

### **Introduction**

Hydraulic fracture (HF) operations have been extensively used over the years to increase the productivity of low-permeability hydrocarbon reservoirs. The intersection of hydraulic fractures with present underground natural fractures is proven as the main factor in increasing the productivity of the shale gas reservoirs (Mayerhofer *et al.*, 2010). Microseismic observations (Mayerhofer *et al.*, 2010) and mined-back downhole samples from field operations (Warpinski and Teufel, 1987) support the

importance of natural fractures and their activation during the operation. Understanding the necessary conditions for activation of the natural fracture, the expected magnitude of slip and enhanced fluid transmissivity, and the impact of this slip on the hydraulic fracture path is a key to understanding the hydraulic fracture process.

Several experimental works have been performed to approach this problem. *Hanson et al. (1980)* conducted HF experiments on bonded faults (using Chloroform) in cubic blocks of Nugget sandstone, Indiana limestone, and PMMA. The HF never crossed PMMA interface even at 13.8 MPa normal stress, while it could cross the bonded fault for Indiana limestone and Nugget sandstone. For un-bonded fault in Indiana limestone, the HF could cross the smooth interface at normal stresses higher than 9.2 MPa (the experiments were in an unconfined condition). The required normal stress for HF to cross the Nugget sandstone fault was 6.9 MPa. In an additional experiment on the sandstone, by roughening the fault surface the HF could cross the interface at 4.6 MPa. The authors did not report the surface roughness or the fault surface's coefficient of friction. They also bonded blocks with different materials. The HF could cross from PMMA to limestone and from Nugget sandstone to limestone but not the other way around. In a later study on Indiana limestone blocks and same experimental configuration, *Thorpe et al. (1986)* studied the so called "step-cracks". By inserting a strip of 0.75 inches wide lubricant, they observed the HF to pass along this reduced friction section and then cross the interface with an offset. The step-cracks have been observed in mine-back experiments by *Warpinski et al. (1982)* in tuff at Nevada Test Site. They have also been experimentally observed in wedged tensile fracture experiments on limestone and gypsum approaching an inclined fault (*Goldstein and Osipenko, 2015*). Hydraulic fracture on blocks of Wondabyne sandstone also revealed a step-crack of 10-15 mm at an approach angle of  $30^{\circ}$  (*Bunger et al., 2015*).

Alongside the experiments, several cross/arrest criteria have also been developed. Blanton (1982, 1986) analyzed the interaction problem by considering the competition between material's tensile strength and sliding of a Coulomb type frictional interface. He evaluated his proposed criterion by experiments on blocks of Devonian shale and hydrostone at various fault orientation angles of 30, 45, 60, and 90 degrees. The main outcome of this analysis was an asymptotic fault angle below which the hydraulic fracture does not cross the fault. This angle depends on the interface's static coefficient of friction,  $\mu$ . Renshaw and Pollard (1995) presented a theoretical criterion for crossing of a tensile fracture through an orthogonal frictional interface. They considered the competition between the stress intensity singularity at the tensile fracture tip and shear stresses along the interface. Similar to the Blanton model, the interface in their model followed a simple linear friction law, i.e.  $\tau = \mu \cdot \sigma_n$ . Renshaw and Pollard's (1995) criterion has further been extended to consider the non-orthogonal interfaces (Gu et al., 2012) and the interface's cohesive strength (Sarmadivaleh and Rasouli, 2014). This problem has also been approached numerically by various authors. The reader is referred to Wang et al. (2014), Taheri et al. (2016), Chen et al. (2017) for reviews of some of the recent numerical works.

However, some experimental observations contradict these model criteria. One example is seen in the experiments of *Bunger et al. (2015)* where HF crossed a fault with  $15^{\circ}$  orientations. The fault failure during fluid injection cannot be modeled by a simple linear friction law over the entire interface. Instead, the pore fluid diffusion inside the fault during post-slip sliding might play a crucial role which is yet to be understood. The fault constitutive behavior, i.e. its stable/unstable sliding could also be quite important. In addition, the fault slip before HF intersection could orient the direction of HF propagation which needs to be better understood. In this report, we investigated the interaction between an approaching HF and an inclined fault in triaxial stress conditions. First, we measured the coefficient of friction by sliding experiments. We then performed hydraulic fracture experiments on samples containing both a borehole and an inclined fault. By means of a high acquisition rate of acoustic emissions, pore pressure, and stresses, the dynamic processes during this interaction are studied. Finally, the observations are compared to existing crossing criteria and the limitations and contradictions are discussed.

## Experimental Procedure

Cylindrical samples of PMMA and Solnhofen limestone were prepared and the end surfaces were ground parallel. The cylinders have a diameter of 1.5 inches and a length between 2.7 and 2.9 inches. Faults with specified orientations were then saw cut and the fault surface were finely polished down to a sand paper level of P1000. The root mean square (rms) surface roughness is measured as  $1.07 \mu\text{m}$  (see Appendix C). The fault orientations include 30, 45, 60, and 90 degrees with respect to the vertical axis (see Figure 1). A blind borehole with a diameter of 2.92 mm was then drilled into the top half of the cylinder. The bottom of borehole in all samples has a constant vertical distance of 6 mm from the fault surface as shown schematically in Figure 1 along with other sample dimensions. Four piezoelectric transducers were mounted on the sample. Two transducers are mounted (epoxied using conductive epoxy) inside the top and bottom spacers. The two radial transducers are mounted (epoxied using conductive epoxy) on bronze couplants diametrically opposite to each other; one face of the bronze piece is machined to a surface curvature of 1.5 inches in order to conform to the sample surface. The bronze couplants are epoxied through the polyurethane jacket. Therefore, confining pressure provides the coupling between transducer/sample. The piezoelectric ceramics are p-wave type transducers with resonant frequency of 1.5 MHz. The AE transducers are calibrated with respect to the moment magnitude of ball drop AE events. The procedure is explained in details in Appendix A2. One vertical strain gauge is also mounted on the surface of the bottom half of sample (foot-wall) below the fault surface to record the temporal vertical stress variations. A pore pressure transducer outside of the pressure vessel records the pressure

in the borehole. The frequency response of the pore pressure transducer, evaluated in Appendix A1, act as a low-pass filter at 1.4 kHz. A Doppler laser vibrometer that is focused on the load point records the vertical vibrations of the system's piston and captures the displacement/velocity. The vibrometer is calibrated by the provider company (Polytec Inc.) with a signal output in mm/s/V. The experimental data is recorded independently on two different systems. The mechanical data including the confining pressure, axial stress, pore volume, and vertical displacement is recorded with a sampling rate of 1 Hz. The piezoelectric sensors, strain gauge, pore pressure transducer, and laser vibrometer response is recorded using a TraNET EPC-32 acquisition system (Elsys Inc.) with trigger-based sampling rate of 5 MHz. The acquisitions are conducted in a specific mode developed by Elsys Inc., so-called ECR mode. In this mode, the data are acquired and streamed to disk with no dead-time which is a major drawback in typical trigger-based acquisition systems. Therefore, it ensures no data loss at the 5 MHz sampling rate. The acoustic emission (AE) response is preamplified by either 30 or 54 dB preamplifiers; the strain gauge and pressure transducer response were input into a signal conditioner (gain $\times$ 100 and excitation voltage 2V) before acquisition.

The pore pressure transducer records the pore pressure 17 inches away from the borehole. The laser vibrometer also records the load point motion velocity outside of the vessel, 16 inches away from the sample. In order to synchronize these measurements with acoustic emission and axial stresses from strain gauge, the pore pressure and vibrometer velocity readings were time-shifted considering the travel time for compressional wave in water line and steel parts by 288 and 71  $\mu$ sec, respectively.

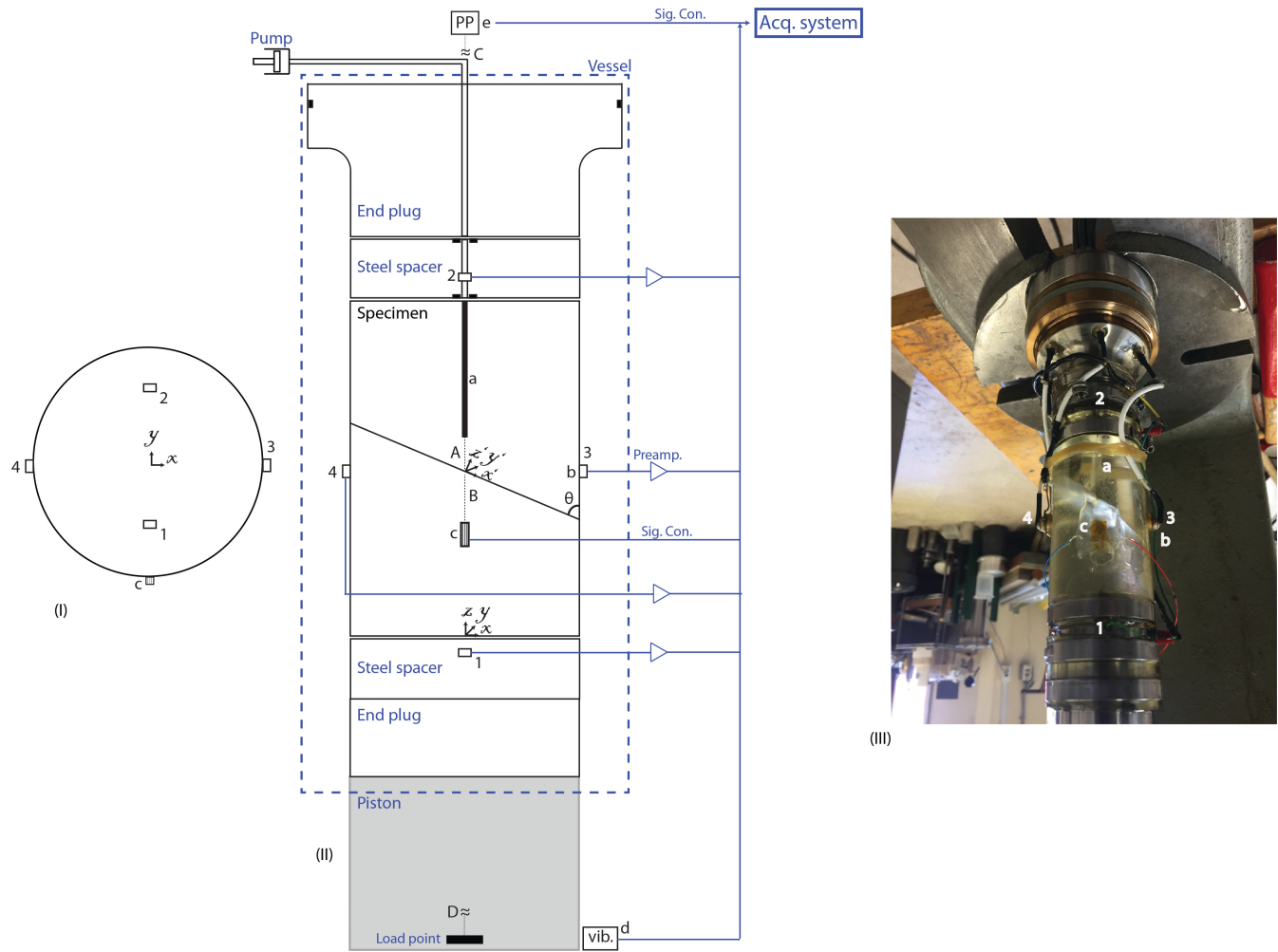


**Figure 1. Schematic (I and II) and real picture (III) for the geometry of sample and sensors during the experiments. Note that the schematic is not drawn in scale. (a) is a blind borehole drilled in the top half of sample close to a fault with orientation of  $\theta$ . Two coordinate systems are shown with their origins as  $xyz$  and  $x'y'z'$ ;  $x'y'z'$  is obtained by clockwise rotation of  $xyz$  wrt to  $y$  axis by  $90-\theta$ . (b) is the AE transducer and numbers correspond to the transducer number. (c) is the strain gauge mounted on the sample surface and measuring the vertical stress. (d) is the Doppler laser vibrometer measuring piston's vertical velocity at the load point. (e) is the pore pressure transducer measuring the borehole pressure. (A) is the vertical distance between borehole bottom and fault which is always 6 mm. (B) is the vertical distance between strain gauge center and fault which is always 0.6 inches. (C) is the distance between pore pressure transducer and borehole bottom which is 17 inches. (D) is the distance between load point and sample which is 16 inches. The AE signal is fed to a preamplifier, the pore pressure and strain gauge are fed to a signal conditioner. The vibrometer which is calibrated by provider company has a signal output of mm/s/V. The whole dynamic data is then acquired by the acquisition system.**

The confining pressure in all experiments is maintained at a constant value of 5 MPa. We conducted two separate types of experiments. In **sliding experiments**, a constant axial shortening rate of  $2 \mu\text{m}/\text{sec}$  was applied. This led to relative sliding on the fault surface in the sample. The axial stress during the experiment was corrected for the contact area losses during the fault sliding (Tembe et al., 2010). For the triaxial stress conditions with  $\sigma_1$  and  $\sigma_3$  as the maximum and minimum *in-situ* stresses, the resolved shear ( $\tau$ ) and normal ( $\sigma_n$ ) stresses on a fault plane with orientation of  $\theta$  with respect to the maximum stress are obtained as:

$$\tau = 0.5 (\sigma_1 - \sigma_3) \sin(2\theta) \quad (1)$$

$$\sigma_n = \sigma_3 + 0.5 (\sigma_1 - \sigma_3) (1 - \cos(2\theta)) \quad (2)$$

The resolved shear and normal stresses on the fault plane can then be calculated and the coefficient of friction is obtained as the ratio of maximum shear stress over normal stress for a certain fault angle (Lockner et al., 2017).

In the second type, **hydraulic fracture**, the axial stress was increased by advancing the piston and then locking it in place when the desired stress was achieved. Throughout this paper, we use the “differential stress” term which refers to the difference between the maximum ( $\sigma_1$ ) and minimum ( $\sigma_1$ ) *in-situ* stresses. The pore pressure inside the borehole was then raised by injecting deionized water under constant injection rate of  $2.6 \text{ cm}^3/\text{min}$ . After a critical pore pressure, i.e. breakdown pressure (BP), the hydraulic fracture initiated and propagated towards the fault.

## Sliding Experiments

During the sliding of fault surfaces under constant axial shortening rate, either stable or unstable sliding (stick-slip) can occur. The stable/unstable sliding between bare fault surfaces is governed by the rock type and its saturation state, strain rate, normal stress, and the loading machine stiffness which contributes to this instability (*Byerlee and Brace, 1968*). Prior to HF experiments, the oriented fault surfaces ( $\theta < 90$ ) were briefly slid (less than 1 mm slip along the fault) and the sliding was recorded as explained in the previous section. The maximum slip velocity and total slip were estimated from load point velocity and slip duration ( $d = \int v \cdot dt$ ). The moment magnitude of the event was estimated from AE signals. The stress drop after sliding is derived from strain gauge stress readings. Table 1 shows the experimental conditions for the sliding experiments. As a standard in reporting the coefficient of friction, we adapted the following procedure: for stable sliding, the coefficient of friction,  $\mu$ , is reported at the axial shortening displacement of 0.2 mm. For stick-slip sliding,  $\mu$  is obtained by averaging the first three peaks for stick-slip events. Again, all these experiments were conducted under a constant axial shortening rate of 2  $\mu\text{m}/\text{sec}$ .

**Table 1. The experimental conditions and obtained parameters for sliding experiments. The  $\mu$  for PMMA experiments with stick-slip behavior is reported by averaging 3 events. The  $\mu$  for Solnhofen limestone with stable sliding is reported by its value at 0.2 mm axial shortening. For experiment names, PM stands for PMMA. SH stands for Solnhofen limestone. The number corresponds to the fault orientation. Note that the confining pressure was constant and equal to 5 MPa for these experiments. The axial shortening rate was also 2  $\mu\text{m}/\text{sec}$ . SD stands for stress drop.**

Experiment Name	$\mu$	Slip velocity, mm/s	Slip Duration, $\mu\text{s}$	Slip, $\mu\text{m}$	SD, MPa	$M_0$
PM30	0.30 $\pm$ 0.03	84.0	123	5.39	2.2	-5.69
PM45	0.30 $\pm$ 0.02	72.6	114	4.69	2.1	-
PM60	0.24 $\pm$ 0.02	-	-	-	2.2	-
SH30	0.12	NA	NA	NA	NA	NA
SH45	0.21	NA	NA	NA	NA	NA
SH60	0.11	NA	NA	NA	NA	NA

The sliding in PMMA was associated with stick-slip events. The slip velocity during stick-slip events in PMMA reached values of  $\sim 0.1$  m/s for a duration of  $\sim 0.1$  msec (see Table 1). The slip velocity and total slip decreased at increased fault orientation angles. The stress drop also reached values of  $\sim 2$  MPa which is more than 60% of axial pre-peak differential stress level. During the sliding in Solnhofen limestone no slip velocity or stress drop was registered which is expected from stable sliding. Figure 2 shows the evolution of  $\mu$  during a sliding experiment in PMMA and limestone samples for a  $30^\circ$  fault orientation. The variation of  $\mu$  with respect to the fault orientation is also summarized in Figure 2. The coefficient of friction for both PMMA and Solnhofen limestone tends to slightly reduce as the fault angle approaches  $60^\circ$  and becomes less steep. The reduction in  $\mu$  at less steep fault angles has also been previously observed by *Savage et al. (1996)* in granite samples. The saw-cut faults in granite samples showed a maximum  $\mu$  at about  $20$ - $30^\circ$  and a reduction from 0.78 to 0.62 for their largest tested fault angle, i.e.  $50^\circ$ . The coefficient of friction values in Slate by *Donath et al. (1972)* also showed a slight reduction (0.03) by changing the fault orientation from  $30^\circ$  to  $45^\circ$ . It is also worth mentioning that the PMMA  $\mu$  values in our experiments are significantly lower than the values reported by *Dieterich and Kilgore (1994)*. The PMMA fault surfaces in *Dieterich and Kilgore (1994)* with  $\mu=0.75$  with normal stress of 2.5 MPa had a surface finish of #60 grit size ( $3.89 \mu\text{m}$  roughness in Appendix C) compared to our finely-polished and smooth fault surfaces (The fault surfaces are shiny with surface roughness of  $1.07 \mu\text{m}$  in Appendix C). The PMMA fault in *Mclasley (2012)* with a surface finish of #600 grit size measured  $\mu=0.57$ . The measured coefficient of friction for limestone in this report is also much lower compared with *Donath et al. (1972)* reported values of 0.72. The limestone fault with an inclination of  $26^\circ$  in *Donath et al. (1972)* was created after triaxial failure of the intact material in which a higher surface roughness is expected compared to the finely polished surfaces in this report. One possible explanation is that the coefficient of friction is sensitive to the surface roughness and is much less for these polished surfaces.

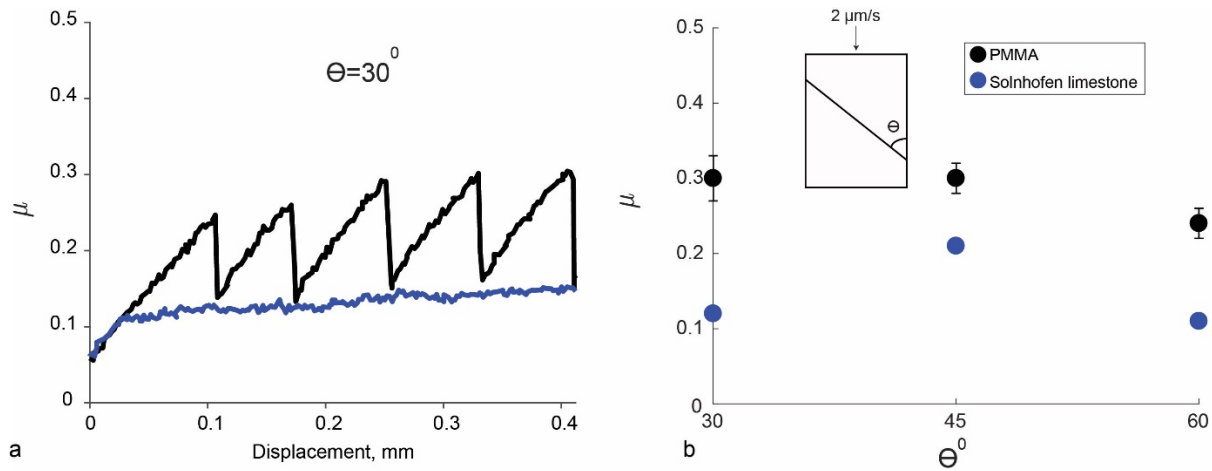


**Figure 2.** (a) Two examples of sliding experiments in Solnhofen limestone and PMMA with a  $30^\circ$  fault angle. The fault surfaces are finely polished (rms roughness=1.07  $\mu\text{m}$ ). The fault in Solnhofen slides stably, while in PMMA it slides with stick-slip events. (b) variation of coefficient of friction with respect to the fault orientation. The  $60^\circ$  fault has the lowest  $\mu$ . For explanation of this variation please refer to the main text.

Figure 3 shows an example for AEs during a stick-slip event for a  $30^\circ$  PMMA fault. The stick-slip event generates AE signals and is associated with a partial post-slip stress drop. The moment magnitude of the AE event was estimated using calibration from a ball drop experiment (see Appendix A2). In this experiment, the AE signal was preamplified by 30 dB, unlike all other experiments and ball drop tests in the Appendix (which had a preamplification of 54 dB). So, the entire slip event could be captured by AE transducers; while the slip event in other experiments was clipped (went off-scaled) as we will see in the next section.

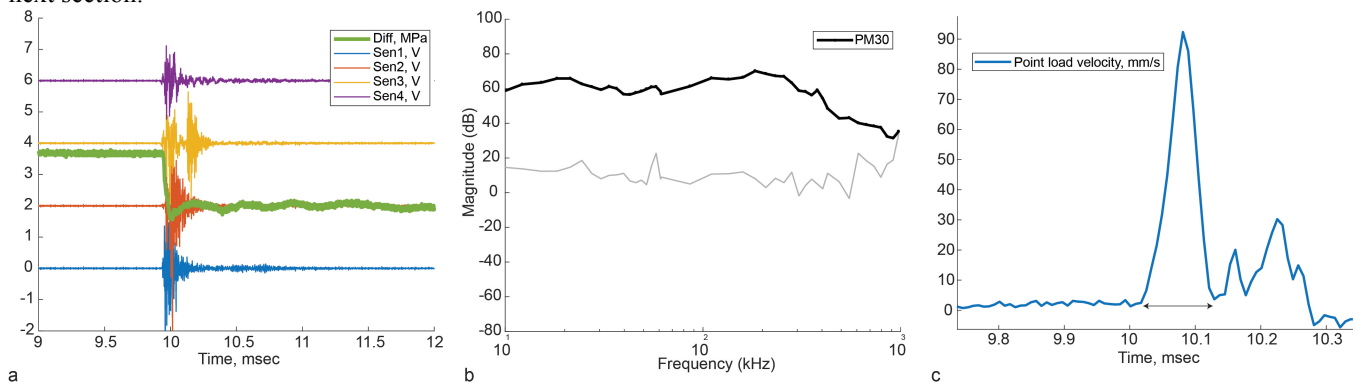


**Figure 3.** (a) The AE events and stress drop from piezoelectric transducers and strain gauge readings during a stick-slip event in PMMA sample with  $30^\circ$  fault orientation (PM30 in Table 1). The position of AE sensors and strain gauge is described in Figure 1. (b) The AE event spectrum averaged over 4 sensors. We use the ball drop experiment (Figure A2) to estimate the moment magnitude,  $M$ , of the stick-slip event. Note that the pre-amplification for this event is 30 dB which is different from ball drop and all other experiments with pre-amplification of 54 dB. Therefore, the AE signals do not go off-scaled like slip events in Figure 4. The gray line also shows the background noise spectrum. Notice the good signal-to-noise ratio for a wide frequency band. Local peaks observed in the signal spectrum coincide with the noise spectrum (c) Doppler laser vibrometer velocity response for a PM30, but a different event than (a). The slip event duration is 116  $\mu\text{s}$  as shown by double-sided arrow. The total slip along the fault is considered as the area under this curve for the slip duration divided by the  $\cos(\theta)$ .

The time window for deriving the signal spectrum is selected so that the entire event is captured. Based on trial in these stick-slip experiments, a 2 ms time window is long enough to represent the event with the middle of the time window at the signal peak amplitude. The laser vibrometer velocity recording is also shown for a stick-slip event. Once again, the vibrometer reads the vertical motion of the piston at the load point outside of the pressure vessel, far from sample. However, it is useful to derive the slip duration (similar to Lockner et al., 2017) and total slip along the fault.

## Hydraulic Fracture Experiments

The pressurized fluid inside the borehole results in initiation of a hydraulic fracture at the borehole wall. It is generally thought that the hydraulic fracture initiates as a tensile mode fracture (Haimson and Fairhurst, 1969; Detournay and Cheng, 1992). Further propagation of HF under either Mode I or mixed I, II modes depends on the local stresses and discontinuities in the rock (Hanson et al., 1980). The designed experiments in this section evaluate the propagation and approach of HF to a neighboring fault. Figure 4 illustrates an example for the recorded events during a hydraulic fracture experiment in PMMA

with a  $30^\circ$  fault. Water is injected at a constant rate of  $2.6 \text{ cm}^3/\text{min}$ . Based on the high rate recorded response, there are some notable characteristics during the HF experiment. The slip on the fault can be detected independently by vibrometer, strain gauge, and acoustic emission signals. It results in an abrupt change in vibrometer velocity, significant generated acoustic signal (The signal goes off-scale and clipped), and a partial stress drop. The abrupt drop in pore pressure is associated with the slip on the fault. The pore pressure then drops to the confining pressure value as the pore fluid reaches the sample jacket. The AE transducers also record a series of events some  $100\text{'s } \mu\text{sec}$  before the major slip (Figure 4b). These are HF initiation and propagation events detected as AEs before the HF intersects the fault. For obtaining the moment magnitude of HF events, we consider only the initiation events; we select a time-window equal to twice that of the rise time of initiation event. The center of this window is at the peak amplitude (see green arrow in Figure 4 which shows the time of HF initiation). Therefore, in PMMA the hydraulic fracture created a significant slip event after intersecting the fault.

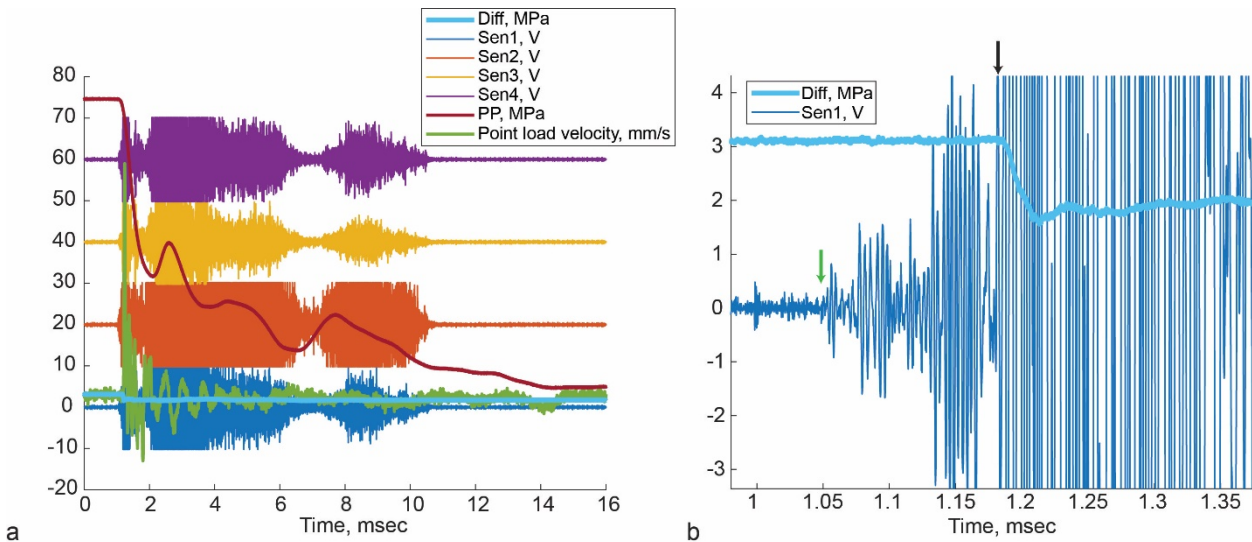


**Figure 4. High acquisition rate recordings during a hydraulic fracture experiment in a PMMA sample with a  $30^\circ$  fault (PM30-3 in Table 2). (a) the AE, stress, and pore pressure readings. The fault slip event after HF intersection is expressed as a burst in AE signals, stress drop, and abrupt decrease in pore pressure. Note that the pore pressure and vibrometer readings are time-shifted based on the time for the distance between reading point and the sample. (b) magnified view of AE signal in one of the transducers (Sen1) and differential stress drop. AE sensors detect HF initiation signals (green arrow) about  $130 \mu\text{sec}$  prior to the slip event (black arrow).**

The hydraulic fracture was also arrested at fault orientations of  $45^\circ$  and  $60^\circ$  and  $90^\circ$  and resulted in either sliding or opening of the fault. The AE transducers can, in fact, detect HF events prior to the fault slip. With certain assumptions, we can estimate the HF propagation velocity before intersecting the fault: HF initiates at the borehole bottom which, in all cases, is 6 mm away from the fault surface along the vertical axis. The HF travels vertically towards the fault; this hypothesis is supported by the fact that the breakdown pressure is significantly influenced by the differential stress (see Figure 6). Therefore, the axial stress is the direction of HF propagation (*Haimson and Fairhurst, 1969*). The average propagation velocity of HF in PMMA experiment is  $44 \text{ m/sec}$ .

Figure 5 shows an example for a hydraulic fracture experiment in Solnhofen limestone. Similar to PMMA experiments, the intersection of HF and fault here is also associated with AE signal burst, pore pressure drop, slip velocity increase, and stress drop. The AE burst during the fault slip, on the other hand is not as noisy as the case of PMMA. Also, the post-slip stress drop is not as significant as the case of PMMA. The HF was able to cross the fault with a subtle fault sliding with slip velocity of  $0.5 \text{ mm/sec}$ . The HF propagation velocity based on AE events was  $12.6 \text{ m/sec}$ .

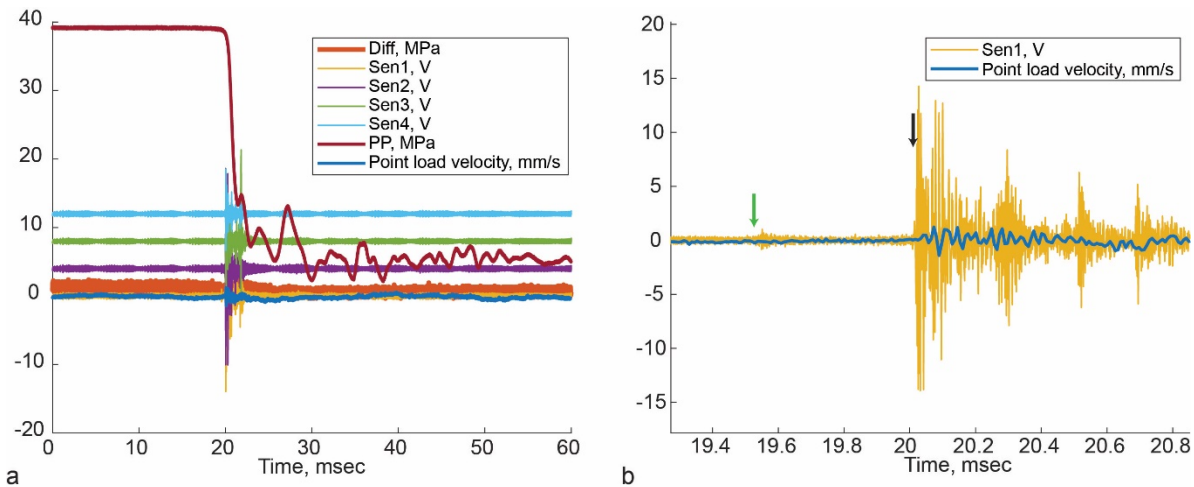


**Figure 5.** Hydraulic fracture experiment in a Solnhofen limestone sample with a  $30^{\circ}$  fault (SH30-1 in Table 2). For explanation of sensors response please refer to Figure 4 caption. The fault slip is associated with a burst in AE (black arrow) and slip velocity. Again, here we observe the HF event prior to slip event in AE signals (green arrow). We use the time difference between these two events to estimate the HF average propagation velocity before intersecting the fault. This velocity is 12.6 m/s in this case. Note the less noisy AE, smaller slip velocity, shorter slip duration, and smaller stress drop compared to Figure 4.

The HF was able to cross the fault to the other side of fault at orientations of  $30^{\circ}$ ,  $45^{\circ}$ , and  $90^{\circ}$ , with an exception at  $60^{\circ}$ . The results of HF experiments are summarized in Table 2. The variation of breakdown pressure and HF crossing/arrest is also plotted in Figure 6. The HF in PMMA was arrested by fault for all orientations and differential stresses. The experimental studies by Hanson et al. (1980) on PMMA-PMMA interface blocks with differential stresses of 14 MPa have resulted in the same conclusion. This observation has an implication for modeling the hydraulic fracture at the interface: the crossed Mode I fracture is not a continuation of previously propagating fracture and needs to be re-initiated at the other side of interface.

For the triaxial stress conditions with the maximum vertical stress, in the absence of fault the hydraulic fracture preferentially initiates along the borehole axis, with no preference in azimuth. In these experiments, the presence of fault seems to impose a preferred azimuth for HF, i.e. normal to the fault strike or parallel to dip (see Figure 6). The breakdown pressure value for both PMMA and Solnhofen limestone has a peak at  $30^{\circ}$ . In contrast to PMMA, HF was able to cross the fault at almost all fault orientations and differential stresses. The Brazilian test measurements and hydraulic fracturing experiments give a tensile strength of 16 MPa for Solnhofen limestone (Mighani et al., 2015), a value consistent with results from HF experiment in a sample with only a borehole. The tensile strength of PMMA is also measured as 58 MPa in the hydraulic fracture experiment.

The HFs in our experiments have propagation velocities on the order of  $10^2$ 's of m/s (see Table 2), much faster than the velocities measured in some other tests. For example, Lockner and Byerlee (1977) measured velocities of 0.5 mm/sec in Weber sandstone for slow injection rates of 0.02 cc/min. The very low permeability in Solnhofen and PMMA can explain this difference. Depending on the relative magnitude of rock matrix diffusivity and the fluid injection rate, diffusion of the fluid into the region surrounding a fracture can decrease the local effective stress, aid the tensile fracture, reduce the breakdown pressure and increase the speed of the mode I fracture (Detournay and Cheng, 1992).

**Table 2.** Experimental conditions for hydraulic fracture experiments. The experiment's name is adapted as material (PM for PMMA and SH for Solnhofen)-fault angle (degrees)-differential stress (MPa). DS: Differential stress prior to HF. BP: Breakdown pressure. SD, Stress drop. All tests were run at a constant confining pressure of 5 MPa.

Experiment Name	DS, MPa	BP, MPa	HF velocity, m/s	Slip velocity, mm/s	Slip Duration, $\mu$ s	Slip, $\mu$ m	SD, MPa	Interaction
PM30-3	3	76	44.1	59.0	121	3.51	1.4	Arrest
PM45-3	3	69	36.8	39.1	165	2.56	1.2	Arrest
PM45-5	5	71	35.3	48.7	116	2.98	1.4	Arrest
PM60-3	3	81	14.9	8.1	112	1.09	1.2	Arrest
PM90-3	3	66	59.9	-	-	-	0.2	Arrest
PM90-70	70	43	10.5	-	-	-	0	Arrest
SH30-1	1	39	12.6	0.5	29.9	0.01	0.5	Cross
SH45-1	1	27	8.8	0.5	34.4	0.02	0	Cross
SH60-1	1	28	39.1	0.3	37.4	0.02	0	Arrest

SH90-1	1	27	10.7	-	-	-	0	Cross
SH90-30	30	29	7.4	-	-	-	0	Cross

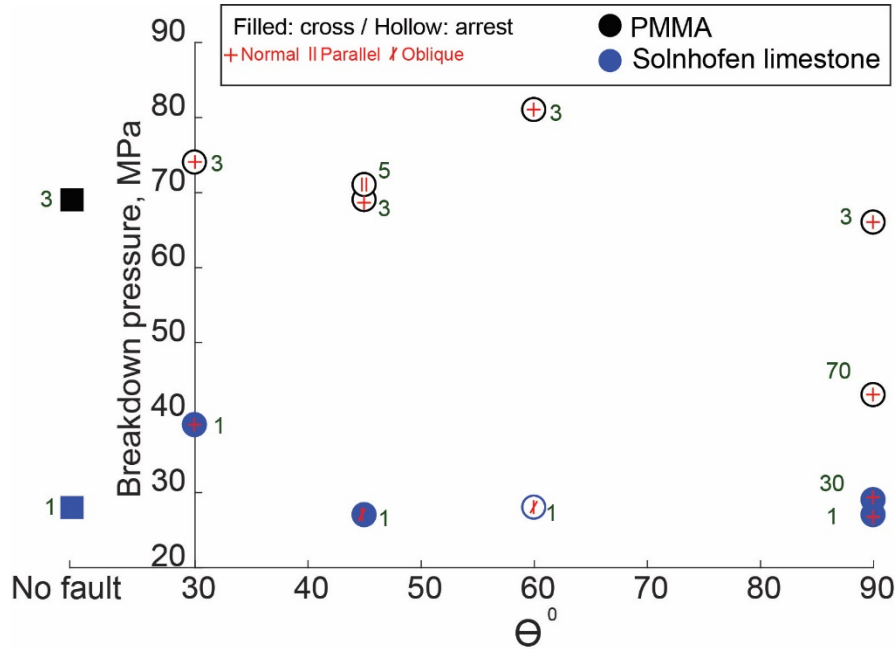
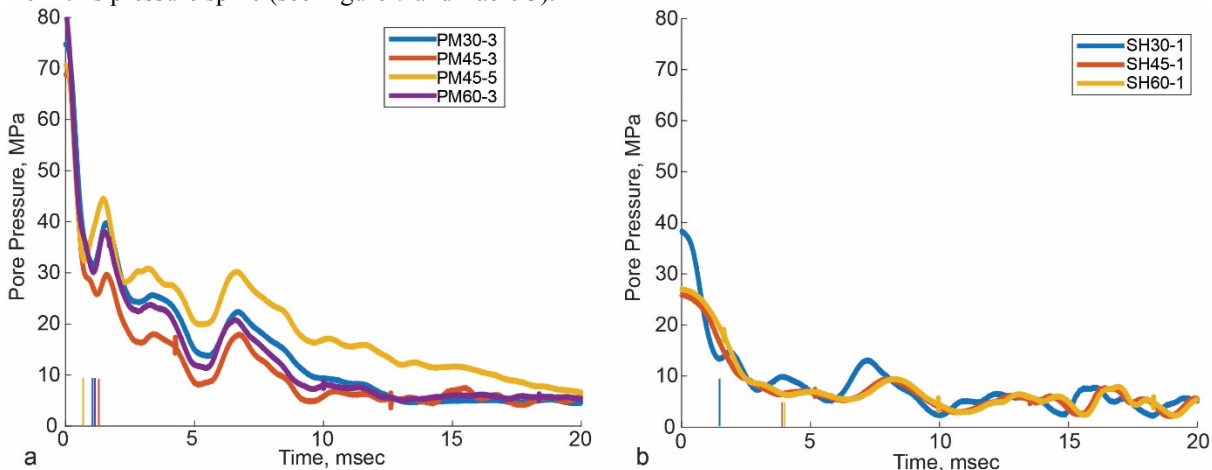


Figure 6. Variation of breakdown pressure as a function of fault orientation for PMMA and Solnhofen limestone. The breakdown pressure value for an intact sample with no fault is also shown for comparison. In addition to breakdown pressures, the crossing/arrest and HF azimuth wrt fault azimuth are also shown. The breakdown pressure for both PMMA and Solnhofen shows a peak at 30°. However, this peak could be within the experimental variations in breakdown pressure values.

The ability of HF to cross the fault in Solnhofen with  $\mu=0.12$ , but to be arrested by the fault in PMMA where  $\mu=0.3$  might seem an unexpected observation. We will discuss this in the remainder of this section. Figure 2 showed the differences in the sliding behavior of faults in Solnhofen limestone compared with PMMA. The fault sliding in PMMA was associated with stick-slip events with significant slip velocity (from vibrometer). In addition to significant stress drop, there was a transient weakening, about 40  $\mu$ sec, before reaching a steady post-slip stress level (see Figures 4 and 5). This is observed in both dry sliding and HF experiments in PMMA. The slip in Solnhofen, on the other hand, is stable during sliding experiments. During HF, a subtle fault sliding occurred with 120 times slower slip velocity. No transient weakening was observed during Solnhofen sliding. We analyze the pore pressure drop to study its decline after the slip occurrence. The pore pressure decline was associated with the fault slip and not the initiation of HF (see Figure 4). The analysis of the HF propagation regime also confirms this observation (Appendix D and Bungler et al., 2005). Based on the experimental parameters, the HF propagates in the toughness-dominated regime where the fluid front and the fracture tip coincide; therefore, we do not expect pressure drops during the HF propagation (see Appendix D). Figure 7 compares the pore pressure drops in all experiments. The pore pressure uniformly declines until the fluid front reaches the jacket. After reaching the jacket it is associated with a back-pressure which results in a jump in pressure response. We can then determine the fluid travel time to reach the fault boundary from this pressure spike (see Figure 7 and Table 3).



**Figure 7. Pore pressure decline in the fault after its intersection with HF in PMMA (a) and Solnhofen limestone (b). The timing of fluid front reaching the fault boundary (diffusion time) is determined on the x axis from the pressure spikes. The diffusion time for limestone fault is generally lower than the PMMA fault.**

The transient diffusion of fluid inside the fault is analogous to the linear heat flow inside an infinite solid bounded by two parallel plates (Carslaw and Jaeger, 1959). Martin (1967) and following him Bernabe and Brace (1990) use this analogy for fluid diffusion inside a porous rock. We use similar derivation for fluid flow inside a fault with a constant hydraulic aperture. The flow inside the fracture follows Poiseuille's law (Kranz et al., 1979). The derivation is explained in Appendix B. Therefore, we can write the following differential form of fluid flow. The left boundary ( $x' = 0$  in Figure 1) or fault inlet (intersection of HF and fault) is insulated with zero pressure gradient. The right boundary or the fault end near the jacket is at constant pressure equal to confining pressure. Notice that  $P$  in the following equation is the fluid net pressure, i.e.  $P_f - P_c$ .

$$\frac{\partial^2 P}{\partial x^2} - \frac{\mu\beta}{K} \frac{\partial P}{\partial t} = 0 \quad (3)$$

$$\frac{\partial P}{\partial x} = 0 \text{ when } x = 0$$

$$P = 0 \text{ when } x = L$$

$$P = P_0 \text{ when } x = 0 \text{ and } t = 0$$

with  $K$  being the fault transmissivity. The fault transmissivity is a cubic function of hydraulic aperture, i.e.  $K = w^3/12$  (Zimmerman, 2012). For more description of the derivation procedure refer to Appendix B. The fluid inside the fault is water with a viscosity of  $\mu = 1$  cp ( $10^{-3}$  Pa.s) and compressibility of  $\beta = 5 \times 10^{-5}$  Pa<sup>-1</sup>. The inlet pressure decline curve is then fit to the observed pore pressure decline. Table 3 shows the derived fault transmissivities and the equivalent hydraulic apertures from the pressure decline curve fit.

**Table 3. Derived fault transmissivities from fitting the inlet pressure decline to the observed pore pressure declines in Figure 7. The derived transmissivity and hydraulic aperture for Solnhofen fault is consistently smaller than PMMA fault.**

Experiment Name	PM30-3	PM45-3	PM45-5	PM60-3	SH30-1	SH45-1	SH60-1
$\Delta P$	71	64	66	76	34	22	23
Diffusion time (msec)	1.04	1.21	0.73	1.10	1.42	3.73	4.09
Transmissivity, $K$ ( $\times 10^{-15}$ m <sup>3</sup> )	6.9	4.9	8.6	7.7	1.2	0.2	0.2
Equivalent Hydraulic Aperture, $w$ ( $\mu$ m)	43.5	38.8	46.9	45.2	24.3	13.3	13.3

The transmissivity values derived for Solnhofen limestone are an order of magnitude smaller than those for PMMA, and, thus, the hydraulic aperture obtained from the transmissivity values for Solnhofen is three times smaller. It is possible that unstable sliding in PMMA was associated with a significant dilation, allowing increased fluid diffusion along the fault. This interpretation is consistent with the results from sliding experiments of Marone et al. (1990) on Ottawa sand fault gouge between the steel plates, where step increases in sliding velocity were accompanied by increased porosity (dilation). Compaction occurred as the velocity was reduced.

## AE Source Analysis

The hydraulic fracture and stick-slip events generated acoustic emission signals on piezoelectric transducers. Both Solnhofen limestone and PMMA did not generate any detectable precursory AE events, unlike stick-slip events in granite which had measurable number of AEs (McLaskey and Lockner, 2014). Figure 8 shows the spectrum of HF events in both Solnhofen limestone and PMMA. The stick-slip event during PMMA sliding experiment is also inserted in this figure for comparison. We can obtain the moment magnitude of the events based on the relative magnitude of spectrum with respect to the instrument response. For a detailed description of obtaining the moment magnitude refer to Appendix A2. The HF event spectrum in PMMA lies above limestone spectrum and has a lower corner frequency. The slip event in PMMA has a much larger magnitude and lower corner frequency than the HF event in PMMA. The lower corner frequency in PMMA HF events compared with limestone can be explained by PMMA's lower Young's modulus. The obtained moment magnitude,  $M$ , for slip event is -5.69. The  $M$  for HF events in PMMA and limestone is -6.95 and -6.8, respectively. The differences between Young's moduli results in lower corner frequency and lower obtained moment magnitude (due to lower force-moment-rate constant in Appendix A2) in PMMA. PMMA also showed a lower corner frequency in ball drop experiments (Figure A2). Therefore, the hydraulic fracture initiation event is 1.4  $M$  scale lower than slip event, so 125 times less strong.

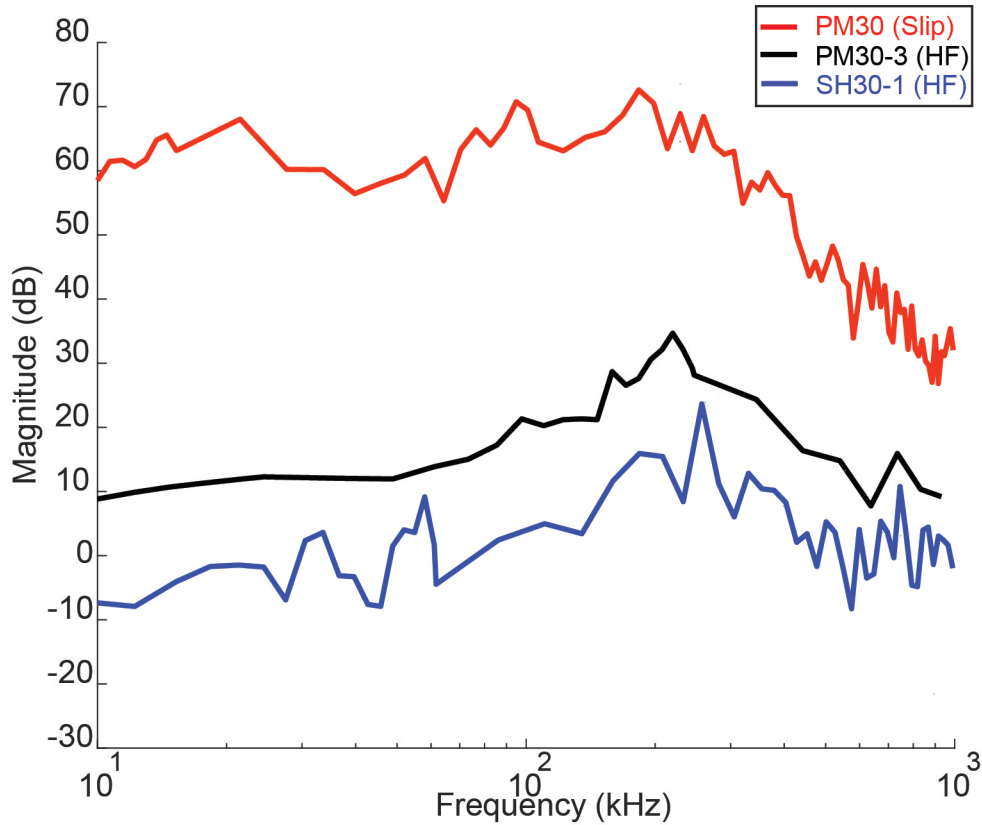


Figure 8. The spectrum of AE events in HF, and sliding experiments. Using the spectrum and derived instrument response and the procedure in Appendix A2 we can obtain the moment magnitude of events. Stick-slip event in PMMA has a moment magnitude of -5.69. The HF events in PMMA and limestone have moment magnitudes of -6.95 and -6.80, respectively.

## Comparison with Cross/Arrest Criteria

The shear activation of a preexisting fault under tectonic stresses is governed by the resolved shear ( $\tau$ ) and normal ( $\sigma_n$ ) stresses on to the fault plane. The necessary condition for the activation of this fault follows the Amonton's law:

$$\tau = \mu(\sigma_n - p_f) \quad (4)$$

with  $\mu$  being the material's static coefficient of friction and  $p_f$  the *in-situ* pore fluid pressure. For a 2D geometry with  $\sigma_1$  and  $\sigma_3$  as the maximum and minimum far-field stresses, the resolved shear and normal stresses on a fault plane with orientation of  $\theta$  with respect to the maximum stress are obtained as:

$$\tau = 0.5 (\sigma_1 - \sigma_3) \sin(2\theta) \quad (5)$$

$$\sigma_n = \sigma_3 + 0.5 (\sigma_1 - \sigma_3) (1 - \cos(2\theta)) \quad (6)$$

By rearranging equation (4) using equations (5) and (6) we can obtain the required stress ratio ( $R$ ) for the fault activation (Sibson, 1985):

$$R = (\sigma_1 - p_f) / (\sigma_3 - p_f) = \frac{(1 + \mu \cot \theta)}{(1 - \mu \tan \theta)} \quad (7)$$

Using equation (7) one can obtain the optimal orientation for fault reactivation,  $\theta^* = (0.5) \text{atan}(1/\mu)$ . By forcing the denominator in eq. (7) to zero,  $R$  approaches infinity. This orientation is the fault lock-up angle and equals  $\theta^r = \text{atan}(1/\mu)$ . For orientations larger than  $\theta^r$  the fault does not slip, unless  $(\sigma_3 - p_f)$  becomes negative, i.e. pore fluid over-pressure. The lock-up angle for coefficient of friction values of 0.12, 0.3, 0.6, 0.8 is  $83^\circ$ ,  $73^\circ$ ,  $60^\circ$ , and  $51^\circ$ , respectively. Based on our observations during the previous sections, the HF in Solnhofen limestone could cross the fault with  $\mu=0.12$  and orientation of  $30^\circ$ , much steeper than the fault lock-up angle. This means that the fault slip under transient pore fluid diffusion does not simply follow equation 4 which assumes constant pore fluid pressure inside fault.

Now we consider the special geometry of an approaching hydraulic fracture to a fault interface. The material properties on both sides of the interface are similar. The hydraulic fracture which has exceeded the material's tensile strength,  $T$ , at the borehole creates a stress field ahead of its tip (*Broek, 1986*). The re-initiation of the hydraulic fracture on the other side of the frictional interface is an appealing assumption to describe the HF crossing after reaching the interface (*Lam and Cleary, 1984*). The re-initiation occurs at a critically-stressed Griffith type flaw due to the stress singularity ahead of the tip of the approaching HF. The necessary condition for the propagation of the hydraulic fracture is:

$$P_{HF} > T + \sigma_3 \quad (8)$$

Two scenarios could be considered for the interaction:

1- The hydraulic fracture reaches the fault and the fluid pressure propagates inside the entire finite length of the fault; therefore, the fluid over-pressurizes the fault and the fault fails either by opening or sliding. In other words, the fault "arrests" the hydraulic fracture.

2- The hydraulic fracture reaches the fault; however, the hydraulic fracture tip singularity is enough to exceed the tensile strength of the material on the opposite side of the fault surface. Therefore, the hydraulic fracture re-initiates on the opposite side of the fault and not necessarily on the same plane as its original plane with some offset. In other words, the hydraulic fractures "crosses" the fault.

Blanton (1982, 1986) approached the problem by considering the competition between material's tensile strength and sliding of a Coulomb type frictional interface. Renshaw and Pollard (1995) and its further extension for non-orthogonal faults by Weng et al. (2014) and Sarmadivaleh and Rassouli (2014) considered the competition between the stress intensity singularity at the HF tip and shear stresses along the interface. Figure 9 shows the cross/arrest predictions based on these criteria including our experimental observations. The extensions of Renshaw and Pollard (1995) for non-orthogonal faults obey similar treatment of the problem. Therefore, here we review only Renshaw and Pollard (1995) criterion. The criteria predict the required differential stress for crossing of the hydraulic fracture.

Equation 9 shows the Renshaw and Pollard criterion:

$$\frac{\sigma_1}{-T + \sigma_3} > \frac{0.35 + 0.35/\mu}{1.06} \quad (9)$$

Blanton criterion is as follows:

$$\sigma_1 - \sigma_3 > \frac{-T}{\cos(2\theta) - b \cdot \sin(2\theta)} \quad (10)$$

with  $b$  having an asymptotic value of:

$$b = \frac{1}{2\pi} \ln \left[ \frac{1 + (1 + e^{\pi/2\mu})^{0.5}}{1 - (1 + e^{\pi/2\mu})^{0.5}} \right]^2 \quad (11)$$

Therefore, the obvious dependency on the material's tensile strength and interface's coefficient of friction are an outcome of these criteria.

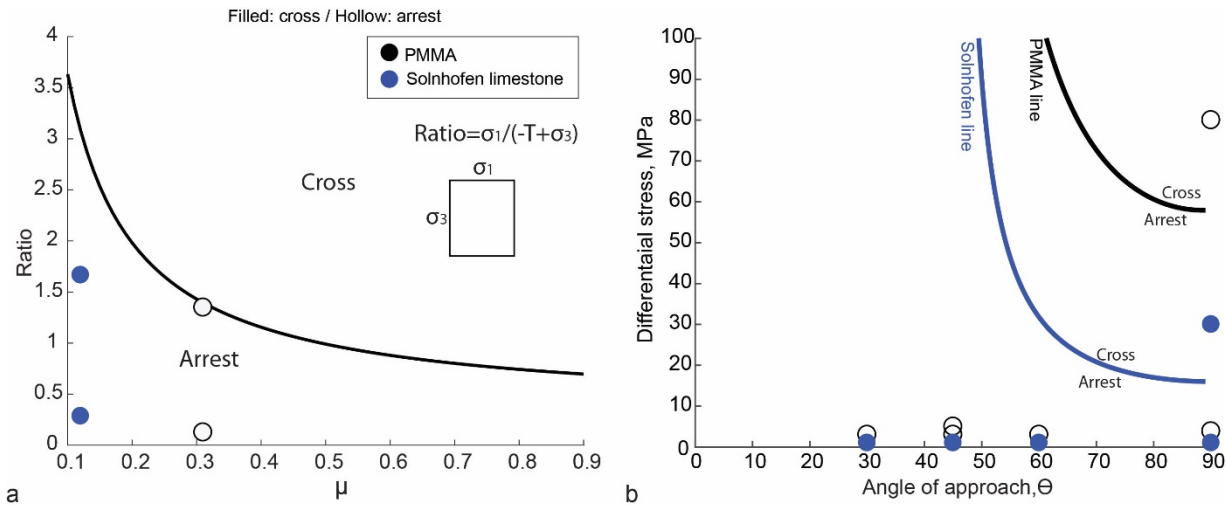


**Figure 9. Existing cross/arrest criteria including our experimental observations. (a) shows Renshaw and Pollard (1995) criterion for an orthogonal fault. The Solnhofen limestone observations apparently contradict the crossing criterion. (b) shows Blanton (1986) cross/arrest criterion for a non-orthogonal fault. There is an asymptotic fault angle below which the HF does not cross the fault. Our observations again contradict the criterion.**

It is shown in Figure 9 that the criteria fail to predict the observations of cross/arrest in our experiments. They could not predict the crossed HF in Solnhofen experiments; they could not also predict the HF arrest by PMMA for a  $90^\circ$  fault and high differential stress. We summarize the hydraulic fracture experiments in the literature in the presence of a fault in Table 4.

**Table 4. Compilation of literature hydraulic fracture experiments with interaction with a fault. The crossing approach angle for fault orientations of less than  $90^\circ$  is also reported.**

	Tensile strength, MPa	Young's modulus, GPa	Poisson's ratio	$\mu$	Fluid viscosity, cp	$\Theta, ^\circ$ (cross $\Theta$ )	Cross DS
Smooth Nugget SS <sup>a</sup>	5.6	30	0.07	0.55	300	90	4.5
Rough Nugget SS <sup>a</sup>	5.6	30	0.07	0.6	300	90	4.5
Smooth Indiana LS <sup>a</sup>	5.3	26	0.12	0.5	300	90	5.5
PMMA <sup>f</sup>	62	2.5	0.33	-	-	90	Not up to 13.8
Rough Indiana LS <sup>a</sup>	5.3	26	0.12	0.62	300	90	3.4
Coconino SS <sup>b,c</sup>	6.4	34.5	0.24	0.68	-	30-90 ( $\geq 60$ )	10.3 (60 <sup>b</sup> ) 6.9 (90 <sup>b</sup> )
Hydrostone <sup>c</sup>	3.1	10	0.22	0.7	-	30-90 ( $\geq 60$ )	15 (60 <sup>b</sup> ) 9 (90 <sup>b</sup> )
Wondabyne SS <sup>d</sup>	3.2	15	0.31	0.76	20,000	15-90 ( $\geq 15$ )	9.8 (15 <sup>b</sup> ), 23 (30 <sup>b</sup> ) 7 (90 <sup>b</sup> )
ABG Gabro <sup>d</sup>	10.9	102	0.27	0.17	30	90	6.8

<sup>a</sup>Anderson (1981) <sup>b</sup>Warpinski and Teufel (1987) <sup>c</sup>Blanton (1986) <sup>d</sup>Bunger et al. (2015) <sup>e</sup>Teufel and Clark (1981) <sup>f</sup>Hanson et al. (1980)

The properties and conditions present in our current experiments differ from earlier work in several important aspects. Many earlier studies conducted on cubic samples were under true triaxial stress conditions, i.e., stress states more comparable to the field operations. Sample dimensions were tens of centimeters (Hanson et al., 1980) to meter (Gu et al., 2012), thus providing much larger fault surfaces during the interaction. Often, earlier studies were performed on sandstone samples with permeabilities larger than a micro-darcy (Warpinski and Teufel, 1987; Bunger et al., 2015) and low tensile strength values, i.e. 3-10 MPa (Blanton, 1986). The permeability favors HF crossing by reducing the effective stress (Detournay and Cheng, 1992), as do the values of coefficient of friction (0.6-0.7) (Blanton, 1982) and the low tensile strengths. In the experiments reported here, the matrix permeability is of order of a nano-darcy and the matrix can be treated as impermeable for our experimental time scales. The coefficient of frictions are quite low and the fault dimensions are small, whereas the tensile strength in both Solnhofen and especially PMMA are quite large by comparison (Table 4). We notice that HF's in recent experiments by Bunger et al. (2015) crossed faults even at orientations of  $15^\circ$ , also contradicting the model criteria.

## Impact of Fault on HF Azimuth

In 8 of 11 experiments, the hydraulic fractures intersected the fault at an azimuth roughly orthogonal to the fault strike, or parallel to dip. In only 1 in 11 experiments was the HF parallel to strike. We have conducted finite element calculations in order to compute the stresses near the borehole. The geometry of the model is shown in Figure 10 which includes a blinded borehole and a fault. The finite element calculations are conducted using PyLith finite element code. For a hollow cylindrical geometry, the tangential and radial stresses inside the solid are independent from the azimuth and only dependent on the radial distance from the internal boundary (Timoshenko and Goodier, 1970). Figure 10 shows the distribution of  $\sigma_{yy}$  near the

borehole for both PMMA and Solnhofen limestone. The boundary and loading conditions are similar to PM30-3 and SH30-1 experiments in Table 2. This figure shows that due to the presence of fault, the near borehole stress symmetry breaks down. Therefore, there is a preferential azimuth for initiation of the hydraulic fracture; it initiates at the maximum tensile region, i.e. perpendicular to the fault strike. Therefore, the presence of fault results in perturbation of local stresses which gives the tensile (hydraulic) fracture preference to propagate normal to its azimuth. Fault-normal joints have also been observed in geological scales in Rough and Rocky Mesa in Utah (Kattenhorn et al., 2000). Displacement Discontinuity modeling (DDM) of an approaching joint to a normal fault also suggests the influence of stressed fault on local stress orientations which affects the joint propagation path (Sheibani, 2013).

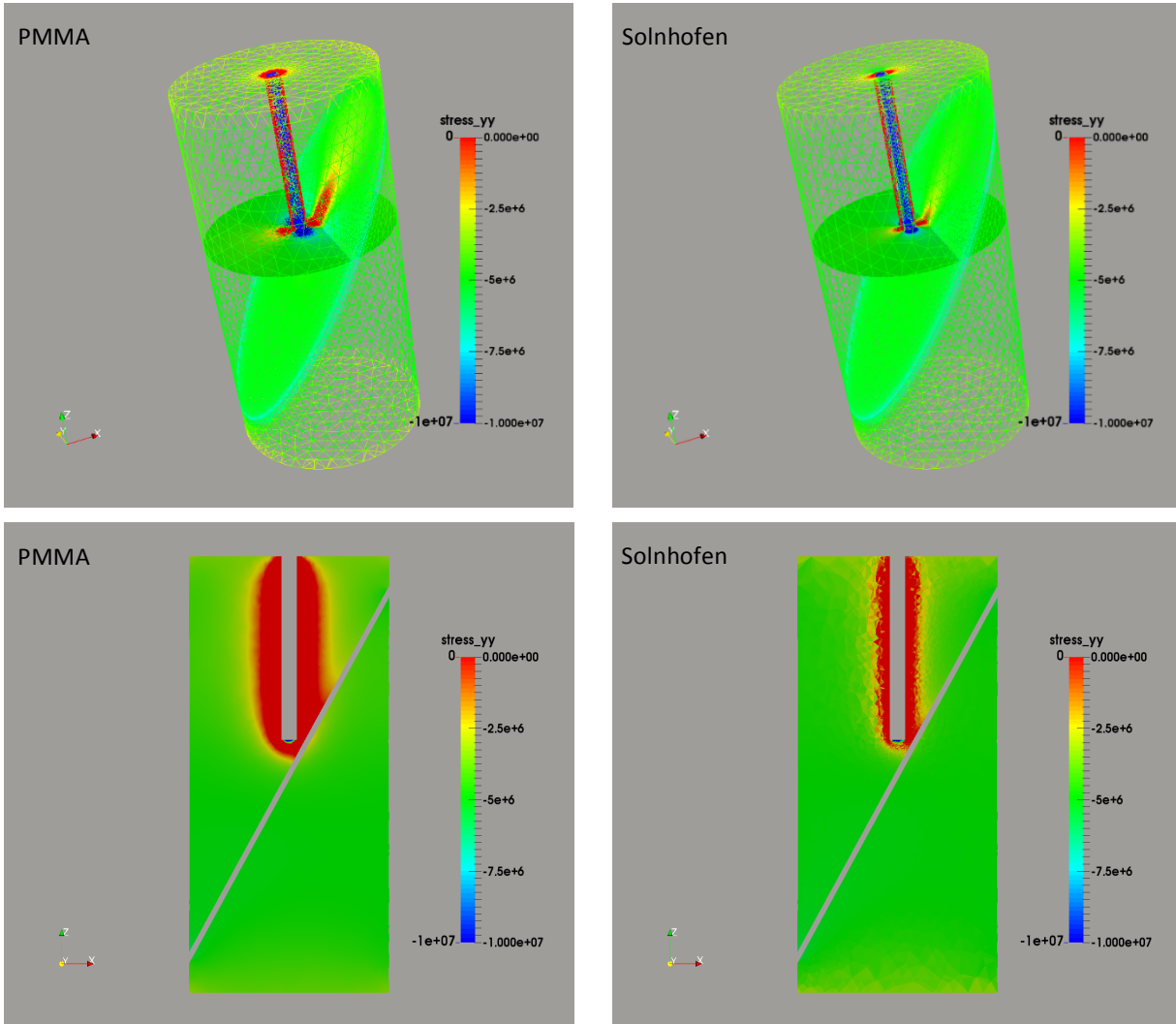


Figure 10. The distribution of  $\sigma_{yy}$  in 3D Finite Element (FE) models of our experimental geometry. Left and right show results for conditions similar to PM30-3 and SH30-1, respectively. The stresses are shown on a cross section intersecting the bottom of borehole and the inclined fault (top) and an axial plane crossing perpendicular to fault azimuth (bottom). The fault in this figure has an inclination of  $30^\circ$  with its strike in y direction. The radial stress is equal to confining pressure, 5 MPa. The borehole is under constant pressure. Tensile stresses are shown by hot, while compressional stresses are shown by cold color. The fault breaks the azimuthal symmetry of stresses making the  $\sigma_{yy}$  more tensile in x direction, i.e. perpendicular to the fault azimuth.

## Conclusions

We designed and conducted a series of experiments to investigate the interaction between a preexisting fault and a hydraulic fracture. The experiments were conducted on PMMA and Solnhofen limestone samples. The sliding experiments showed low  $\mu$  values and different sliding schemes for the limestone (stable) and PMMA (stick-slip). The values of coefficient of friction in this report are low compared to commonly reported values of  $\sim 0.6$ . The measured surface roughness of  $1.07 \mu\text{m}$  for our finely polished fault surface may explain this anomalously low value for both PMMA and limestone. Hydraulic fracture was arrested by the fault in PMMA, and was accompanied by a significant stress drop and slip rate in inclined faults. In contrast,

in Solnhofen limestone, the HF usually crossed the fault. The hydraulic fracture initiated normal to the strike of the fault. The propagation velocity of HF in the experiments could easily reach 10's of m/s. The stick-slip event in PMMA had a moment magnitude of -5.69. The HF event had a moment magnitude of -6.8 (Solnhofen) and -6.95 (PMMA).

The observations cannot be explained based on the existing cross/arrest criteria of Blanton (1986) and Renshaw and Pollard (1995). The criteria underpredict the differential stress required for crossing in PMMA and overpredict this value for Solnhofen. The pore pressure decline after the HF intersection was used to estimate the fluid transmissivity of the fault based on the observed pore pressure decline. The main observations were:

1- In PMMA, the HF was arrested after intersection with fault at all fault orientations and differential stresses. The fault slid with a slip velocity of ~60 mm/s and a significant drop in differential stress (~ 45%). The pore pressure dropped to a much lower value within 1 mseconds after the stick-slip event.

2- The HF in Solnhofen limestone behaved differently. After HF intersection, the fault slid with a slow slip velocity of 0.5 mm/s and a subtle stress drop. The HF was able to cross the fault at almost all fault orientations. The pore pressure decline was longer than PMMA experiments.

The experiments suggest that in order to fully describe the interaction phenomenon, the slip-induced fluid diffusivity needs to be considered. Therefore, the reciprocal behavior of fault sliding and the fluid diffusion as a result of this sliding needs to be considered in order to modify the existing criteria.

## References

- Anderson, G.D. 1981. Effects of friction on hydraulic fracture growth near unbonded interfaces in rocks. *Society of Petroleum Engineers Journal*, 21(01), pp.21-29.
- Blanton, T.L. 1982. An experimental study of interaction between hydraulically induced and pre-existing fractures. In *SPE unconventional gas recovery symposium*. Society of Petroleum Engineers.
- Blanton, T.L. 1986. Propagation of hydraulically and dynamically induced fractures in naturally fractured reservoirs. In *SPE unconventional gas technology symposium*. Society of Petroleum Engineers.
- Broek D. 1986. *Elementary Engineering Fracture Mechanics*. Nijhoff, Boston.
- Bunger, A. P., Jeffrey, R. G., and Detournay, E. 2005. Application of scaling laws to laboratory-scale hydraulic fractures. In *Alaska Rocks 2005, The 40th US Symposium on Rock Mechanics (USRMS)*. American Rock Mechanics Association.
- Bunger, A.P., Kear, J., Jeffrey, R.G., Prioul, R. and Chuprakov, D. 2015. Laboratory investigation of hydraulic fracture growth through weak discontinuities with active ultrasound monitoring. In *13th ISRM International Congress of Rock Mechanics*. International Society for Rock Mechanics.
- Byerlee, J.D. and Brace, W.F. 1968. Stick slip, stable sliding, and earthquakes-effect of rock type, pressure, strain rate, and stiffness. *Journal of Geophysical Research*, 73(18), pp.6031-6037.
- Carslaw, H.S. and Jaeger, J.C. 1959. *Conduction of Heat in Solids*, 2nd ed., Oxford Univ. Press (Clarendon), London.
- Chen, Z., Jeffrey, R.G., Zhang, X. and Kear, J. 2017. Finite-element simulation of a hydraulic fracture interacting with a natural fracture. *SPE Journal*, 22(01), pp.219-234.
- Detournay, E. E., and Cheng. A. E. 1992. Influence of pressurization rate on the magnitude of the breakdown pressure. *The 33th US Symposium on Rock Mechanics (USRMS)*. American Rock Mechanics Association, 1992.
- Goldstein, R.V. and Osipenko, N.M. 2015. Initiation of a secondary crack across a frictional interface. *Engineering Fracture Mechanics*, 140, pp.92-105.
- Gu, H., Weng, X., Lund, J.B., Mack, M.G., Ganguly, U. and Suarez-Rivera, R. 2012. Hydraulic fracture crossing natural fracture at nonorthogonal angles: a criterion and its validation. *SPE Production & Operations*, 27(01), pp.20-26.
- Haimson, B., and Fairhurst, C. 1969. In-situ stress determination at great depth by means of hydraulic fracturing. In *The 11th US Symposium on Rock Mechanics (USRMS)*. American Rock Mechanics Association.
- Hanks, T. C., and H. Kanamori. 1979. A moment magnitude scale, *J. Geophys. Res.* 84, 2348–2350.
- Hanson, M.E., Anderson, G.D. and Shaffer, R.J. 1980. Theoretical and experimental research on hydraulic fracturing. *J Energy Resour Technol Trans ASME*, 102(2), pp.92-8.
- Kattenhorn, S.A., A. Aydin, and D.D. Pollard. 2000. Joints at high angles to normal fault strike: an explanation using 3-D numerical models of fault-perturbed stress field. *Journal of Structural Geology*. 22: 1-23.
- Kranz, R.L., Frankel, A.D., Engelder, T. and Scholz, C.H. 1979. The permeability of whole and jointed Barre granite. In *International Journal of Rock Mechanics and Mining Sciences & Geomechanics Abstracts (Vol. 16, No. 4, pp. 225-234)*.

Pergamon.

- Lam, K.Y. and Cleary, M.P. 1984. Slippage and re-initiation of (hydraulic) fractures at frictional interfaces. *International Journal for Numerical and Analytical Methods in Geomechanics*, 8(6), pp.589-604.
- Lockner, D. and Byerlee, J.D. 1977. Hydrofracture in Weber Sandstone at high confining pressure and differential stress. *Journal of Geophysical research*, 82(14), pp.2018-2026.
- Lockner, D.A., Kilgore, B.D., Beeler, N.M. and Moore, D.E. 2017. The Transition from Frictional Sliding to Shear Melting in Laboratory Stick-Slip Experiments. *Fault Zone Dynamic Processes: Evolution of Fault Properties During Seismic Rupture*, 227, p.105.
- Marone, C., Raleigh, C.B. and Scholz, C.H. 1990. Frictional behavior and constitutive modeling of simulated fault gouge. *Journal of Geophysical Research: Solid Earth*, 95(B5), pp.7007-7025.
- Martin, R. J. 1967. The Effect of Pore Pressure on the Strength of Low Porosity Crystalline Rocks, M. S. thesis, Massachusetts Institute of Technology.
- Mayerhofer, M.J., Lolon, E., Warpinski, N.R., Cipolla, C.L., Walser, D.W. and Rightmire, C.M. 2010. What is stimulated reservoir volume?. *SPE Production & Operations*, 25(01), pp.89-98.
- McLaskey, G.C. and Lockner, D.A. 2014. Preslip and cascade processes initiating laboratory stick slip. *Journal of Geophysical Research: Solid Earth*, 119(8), pp.6323-6336.
- McLaskey, G.C., Lockner, D.A., Kilgore, B.D. and Beeler, N.M. 2015. A robust calibration technique for acoustic emission systems based on momentum transfer from a ball drop. *Bulletin of the Seismological Society of America*, 105(1), pp.257-271.
- Mighani, S., Boulenouar, A., Moradian, Z., Evans, J.B. and Bernabe, Y. 2015. Fluid Compressibility Effects during Hydraulic Fracture: an Opportunity for Gas Fracture Revival. In AGU Fall Meeting Abstracts.
- Renshaw, C.E. and Pollard, D.D. 1995. An experimentally verified criterion for propagation across unbounded frictional interfaces in brittle, linear elastic materials. In *International journal of rock mechanics and mining sciences & geomechanics abstracts* (Vol. 32, No. 3, pp. 237-249). Pergamon.
- Sarmadivaleh, M. and Rasouli, V. 2014. Modified Reinshaw and Pollard criteria for a non-orthogonal cohesive natural interface intersected by an induced fracture. *Rock mechanics and rock engineering*, 47(6), pp.2107-2115.
- Savage, J.C., Lockner, D.A. and Byerlee, J.D. 1996. Failure in laboratory fault models in triaxial tests. *Journal of Geophysical Research: Solid Earth*, 101(B10), pp.22215-22224.
- Sheibani, F. 2013. Solving Three Dimensional Problems in Natural and Hydraulic Fracture Development: Insight from Displacement Discontinuity Modeling. PhD thesis. University of Texas at Austin.
- Sibson, R.H. 1985. A note on fault reactivation. *Journal of Structural Geology* 7, 751-754.
- Taheri-Shakib, J., Ghaderi, A. and Hashemi, A. 2016. Analysis of Interaction Between Hydraulic and Natural Fractures. In *Fracture Mechanics-Properties, Patterns and Behaviours*. InTech.
- Tembe, S., Lockner, D.A. and Wong, T.F. 2010. Effect of clay content and mineralogy on frictional sliding behavior of simulated gouges: Binary and ternary mixtures of quartz, illite, and montmorillonite. *Journal of Geophysical Research: Solid Earth*, 115(B3).
- Teufel, L.W. and Clark, J.A. 1981. Hydraulic-fracture propagation in layered rock: experimental studies of fracture containment (No. SAND-80-2219C; CONF-810518-7). Sandia National Labs., Albuquerque, NM (USA).
- Thorpe, R.K., Hanson, M.E., Anderson, G.D. and Shaffer, R.J. 1982. Step cracks: Theory, experiment, and field observation. In *The 23rd US Symposium on Rock Mechanics (USRMS)*. American Rock Mechanics Association.
- Timoshenko, S.P. and Goodier, J. N. 1970. *Theory of elasticity* - 3rd ed. New York, NY, McGraw-Hill
- Wang, H., Xia, B., Lu, Y., Gong, T. and Zhang, R. 2017. Study on the Propagation Laws of Hydrofractures Meeting a Faulted Structure in the Coal Seam. *Energies*, 10(5), p.654.
- Warpinski, N.R. and Teufel, L.W. 1987. Influence of geologic discontinuities on hydraulic fracture propagation (includes associated papers 17011 and 17074). *Journal of Petroleum Technology*, 39(02), pp.209-220.
- Warpinski, N.R., Finley, S.J., Vollendorf, W.C., O'Brien, M. and Eshom, E. 1982. Interface test series: an in situ study of factors affecting the containment of hydraulic fractures (No. SAND-81-2408). Sandia National Labs., Albuquerque, NM (USA).
- Zimmerman, R.W. 2012. The history and role of the cubic law for fluid flow in fractured rocks. Fall AGY Session H, 71.

## Appendix A – Sensor calibration

### A1-Pore Pressure Transducer

The pore pressure transducer is a Honeywell Inc. Ultra Precision Super TJE model. The nominal frequency response is 2 kHz. In order to evaluate the frequency response of the pore fluid pressurizing system, instead of the sample assembly, a burst disk valve was added to the pressurizing system. The burst disk fails instantaneously at 15 MPa ( $\pm 0.6$  MPa) pressure. We recorded this burst-type event using the same recording system and procedure as the HF events at an acquisition rate of 5 MHz. Figure A1 shows the recording of the transducer for this event. We conducted this experiment for three times. For the first experiment, a long pipe was attached before the disk. The pipe had the same length as the sample assembly line. Water was added behind the disk, so it bursts into a small fluid reservoir, somehow similar to a real HF experiment. For the second experiment, the small fluid reservoir was removed and the disk bursts into air. For the third time, the long pipeline was removed and the disk was still open to air. As can be observed in Figure A1, the instantaneous burst event was recorded at a certain time constant or rise time. This rise time is related to the transducer's frequency response. For instance, the rise time of 705  $\mu\text{sec}$  in Figure A1 corresponds to a frequency response of 1.4 kHz. Therefore, the transducer acts as a low-pass filter and the recorded signal is physically meaningful for frequencies up to 1.4 kHz. The frequency spectrum analysis of the response also shows a flat response up to a corner frequency of 1.4 kHz. The response rolls off abruptly after this corner frequency. It is also noteworthy to mention that the short-pipe system (see Figure A1) has the lowest rise time, i.e. highest frequency response. In other words, by increasing the pipe length and the fluid system volume, the system becomes more compliant which directly affects the system response.

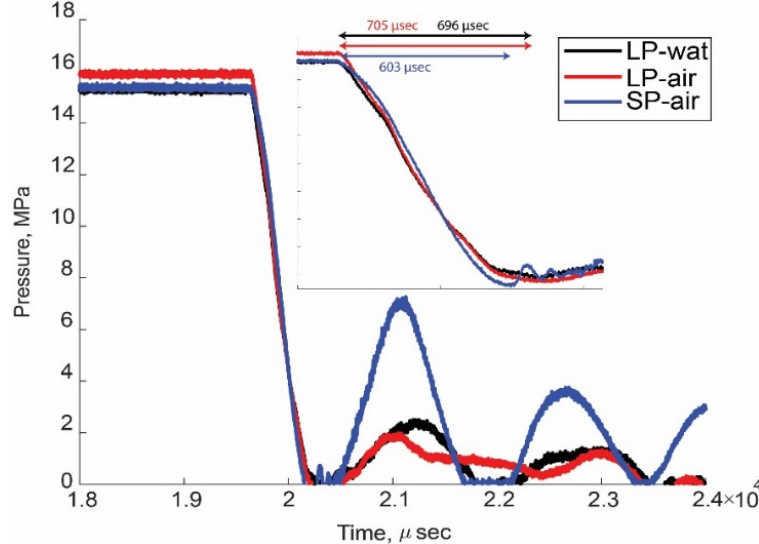
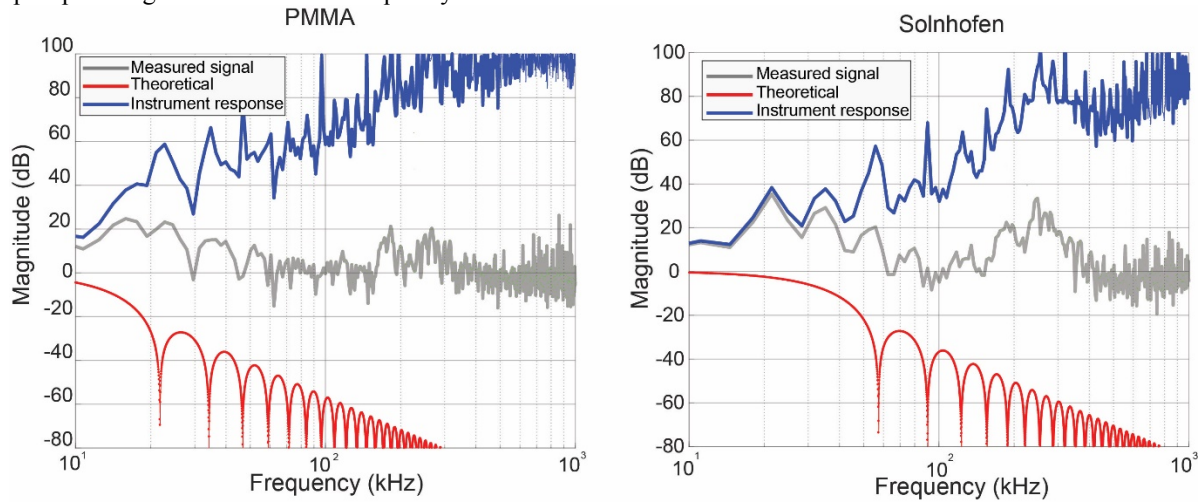


Figure A 1. The pore pressure response for three burst disk tests as explained in the text. The transducer records this instantaneous pressure drop with a rise time between 603-705  $\mu\text{sec}$ , equivalent to frequency response of  $\sim 1.4$  kHz. SP and LP stand for short pipe and long pipe. Wat stands for water. For explanation of these three experiments refer to the text in A1.

### A2-Acoustic Emission Transducers

Following Mclaskey et al. (2015), we calibrated the AE transducers response using ball drop experiments. Note that the notations in this section are similar to Mclaskey et al. (2015), but not necessarily the same. The subscript “*int*” refers to an AE source and “*ext*” refers to a ball drop source. The main motivation behind AE calibrations was to decompose the instrument-apparatus response from the recorded signal and estimate the seismic moment magnitude of the AE events. This way, we use an *external* source (ball drop) to calibrate the *internal* sources (AEs). A steel ball with a diameter of 6.3 mm and mass of  $m = 1.02$  g was dropped from a height of 7 inches onto the center of sample's top surface. These experiments are conducted on bench-top while we applied a vacuum to the jacketed sample to ensure a good sample/sensor coupling. The vacuum acts as if the sample was instead confined to a confining pressure of 1 bar. We recorded the generated AE and the timespan between the ball's first and second impact. We infer the first impact velocity from  $v_1 = \sqrt{2h/g}$  with  $h$  and  $g$  being the free-fall drop height and Earth's gravitational acceleration, respectively. The time difference between the first and the second impact,  $\Delta t$ , helps compute the rebound velocity as  $v_2 = \sqrt{g \cdot \Delta t / 2}$ . The change of momentum is then calculated as  $\Delta P = m(v_2 - v_1)$  where  $v_i$  is a vector. The theoretical impact source spectrum is then obtained from the spectrum of the theoretical force-time function normalized by the change of momentum. The instrument-apparatus response spectrum,  $\Psi_{ext}$ , was then derived by dividing the measured signal by the theoretical spectrums. The spectrums are shown in Fig. A2 for both

PMMA and limestone. The preamplifier is equipped with a 10 kHz high-pass filter. Therefore, the observed and theoretical ball drop impulse signals are shown at frequency lower bound of 10 kHz.



**Figure A 2. Calibration of AE sensors response for their magnitude based on ball drop experiments. (left) shows the calibration for PMMA, while (right) shows the calibration for limestone. The red line is the spectrum of the theoretical ball drop response, the gray is the measured AE signal in the lab. The AE signal spectrum is obtained from a time window of ~2 ms including the event. The blue line is the Instrument response obtained by dividing the Measured signal by the theoretical spectrums. Note that the y axis is in dB units (logarithmic) and dividing between the two responses is simply done by subtracting the two responses.**

The corner frequency in the ball drop experiment for PMMA and limestone is 13, and 34 kHz, respectively. The difference between these corner frequencies which shows in both theoretical and observed ball drop signals owes to the difference in the Young's modulus of these two materials. The ball impact impulse in PMMA with ~3GPa Young's modulus has lower corner frequency compared with the impulse in limestone with ~40 GPa Young's modulus. The change of momentum ( $\Delta P$ ) in the ball drop experiments in PMMA and limestone is 0.0038 and 0.0035 N.s, respectively. The slight difference between the  $\Delta P$  originates from the observed  $\Delta t$  which was 360 and 301 ms for PMMA and limestone, respectively. For internal AE sources, the instrument response,  $\Psi_{int}$ , is obtained from the observed AE signal, i.e.  $S_{int}$  (McLaskey et al., 2015):

$$\Psi_{ext} = C_{FM} \cdot \Psi_{int} \quad (A1)$$

$C_{FM}$  is the force-moment-rate constant which is equal to  $(V_p + V_s)$  with  $V_p$  and  $V_s$  being the material's compressional and shear velocity, respectively.  $C_{FM}$  for PMMA and limestone is 3.9 km/s and 8.9 km/sec, respectively. And, for an AE source:

$$S_{int} = M_0 \cdot \Psi_{int} \quad (A2)$$

Now, combining eq. A1 and A2 we can obtain the moment of the internal AE events as:

$$M_0 = \Delta P \times C_{FM} / (\Psi_{ext} / S_{int}) \quad (A3)$$

And the equivalent moment magnitude is (Hanks and Kanamori, 1979):

$$M = 2/3 \times \log_{10}(M_0) - 6.067 \quad (A4)$$

The equivalent moment magnitude for ball drop experiments in PMMA and limestone is -5.31 and -5.04, respectively.

## Appendix B – 1D Fluid Diffusion Inside Fault

In this appendix, we explain the procedure to derive the governing differential equation for one-dimensional flow of a compressible fluid inside a fracture as an analog to a parallel plate. We follow *Martin's (1967)* scheme to approach this problem. We can write the net rate of fluid flow using Poiseuille's cubic law (Kranz et al., 1979) on closed surface  $S$ :

$$q = \oint_S \frac{w^3}{12\mu} \cdot \nabla p \cdot n \cdot dS = \oint_S \frac{K}{\mu} \cdot \nabla p \cdot n \cdot dS \quad (A1)$$

In this equation,  $q$  represents the flow rate,  $w$ ,  $K$  and  $\mu$  are the fracture hydraulic aperture, fracture transmissivity and fluid viscosity.  $p$  is pressure.  $n$  is the unit vector normal to the surface element  $dS$ . Applying the conservation of mass to the control volume we have:

$$\oint_S \rho \cdot q \cdot n \cdot dS = \frac{\partial m}{\partial t} \quad (\text{A2})$$

This equation expresses that the net outward mass ( $m$ ) flux in the system equals the mass of the entered fluid with a density of  $\rho$  into the system. Now, we divide the above equation by the total volume  $V$  to obtain the mass exchange for a point inside the volume.

$$\lim_{V \rightarrow 0} \frac{1}{V} \iint_S \rho \cdot q \cdot n \cdot ds = \nabla \cdot (\rho q) = -\frac{1}{V} \frac{\partial m}{\partial t} \quad (\text{A3})$$

The mass flux is related to the density variations inside the volume as:

$$\frac{\partial m}{\partial t} = V \frac{\partial \rho}{\partial t} \quad (\text{A4})$$

Therefore, using equation A4, the equation A3 can be rewritten as:

$$\nabla \cdot (\rho q) = -\frac{\partial \rho}{\partial t} \quad (\text{A5})$$

The fluid compressibility,  $\beta$ , is defined as:

$$\beta = \frac{1}{\rho} \frac{\partial \rho}{\partial p} \quad (\text{A6})$$

Now, we rewrite the compressibility equation as:

$$\frac{\partial \rho}{\partial t} = \beta \rho \frac{\partial p}{\partial t} \quad (\text{A7})$$

Now, by replacing the above equation into R.H.S of equation A5 we obtain:

$$\nabla \cdot (\rho q) = \beta \rho \frac{\partial p}{\partial t} \quad (\text{A8})$$

By taking the regional variations of  $\rho$  to be constant (*Martin, 1967*), the divergence equation will appear as:

$$\nabla \cdot (q) = \beta \frac{\partial p}{\partial t} \quad (\text{A9})$$

Now, we integrate the equation A9 over the volume to obtain the cumulative outward mass flux.

$$q = \iiint_R \beta \cdot \frac{\partial p}{\partial t} \cdot dV \quad (\text{A10})$$

Now, we equate this with the Poiseuille inward flow rate:

$$\iiint_R \beta \cdot \frac{\partial p}{\partial t} \cdot dV = \oint_S \frac{K}{\mu} \cdot \nabla p \cdot n \cdot dS \quad (\text{A11})$$

Using divergence theorem, we can write the R.H.S as:

$$\oint_S \frac{K}{\mu} \cdot \nabla p \cdot n \cdot dS = \iiint_R \frac{K}{\mu} \cdot \nabla^2 p \cdot dV \quad (\text{A12})$$

Therefore, we can write A11 as:

$$\iiint_R \left[ \frac{K}{\mu} \cdot \nabla^2 p - \beta \cdot \frac{\partial p}{\partial t} \right] \cdot dV = 0 \quad (\text{A13})$$

Assuming no source or sink, the term inside the integral should be zero. Therefore, we will have:

$$\nabla^2 p = \frac{\beta \mu}{K} \frac{\partial p}{\partial t} \quad (\text{A14})$$

We can solve this differential equation using either numerical methods or analytical solution (*Carslaw and Jaeger, 1959*). Notice again  $K$  is the fracture transmissivity and not permeability. The fracture permeability can be easily obtained from the hydraulic aperture (*Kranz et al., 1979*).

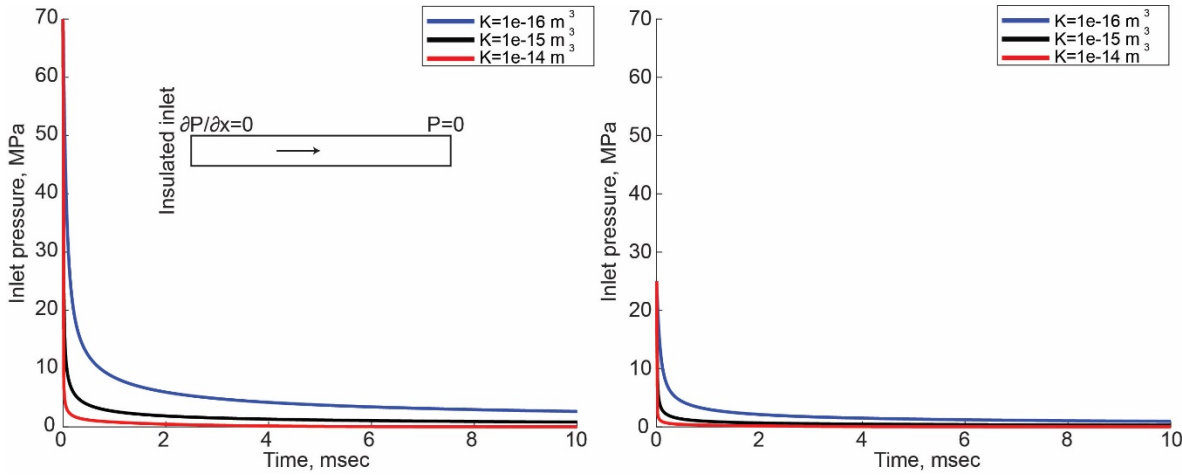


Figure B 1. The decline of left boundary (inlet) during fluid diffusion inside a 1D fracture (analog to a parallel plate). The left curve shows the pressure decline from 70 MPa initial pressure. The right curve shows this decline from a 25 MPa initial pressure. Different curves represent different fault transmissivities in units of  $\text{m}^3$ .

## Appendix C – Surface roughness measurement of faults

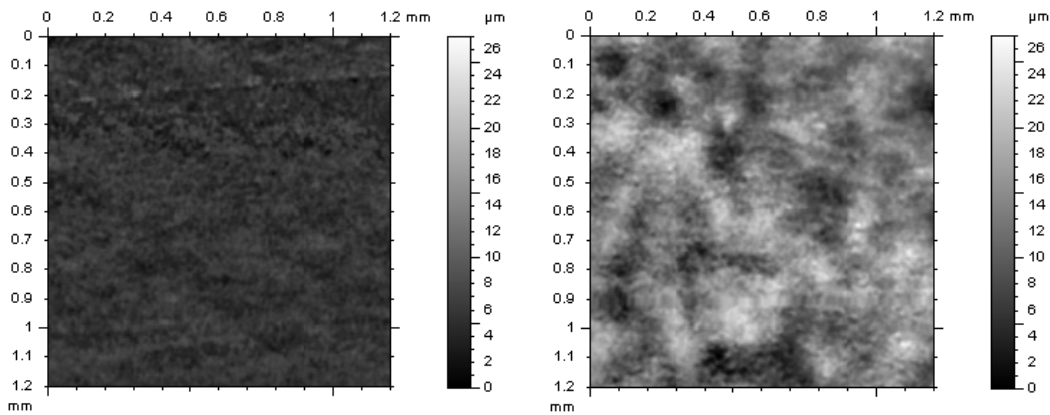


Figure C 1. Surface roughness measurement of a smooth fault (left) and a rough fault (right) surface in Solnhofen limestone. The measurement is conducted using a Talyscan 150 (Taylor Hubson Ltd.) surface profilometer. The surface height is scanned in  $3 \mu\text{m}$  steps over a surface area of  $1.2 \text{ mm} \times 1.2 \text{ mm}$ . The height measurement resolution is  $20 \text{ nm}$ . The surface roughness data have been processed to remove rigid-body tilt and an  $800 \mu\text{m}$  Gaussian filter has been applied to remove the long-wavelength waviness. Left shows the surface of a smooth fault after polishing with a sand paper down to level of P1000 similar to all other experiments in this report. Right shows the surface of a fault with surface finish of #60 grit size. The measured rms surface roughness for left surface is  $1.07 \mu\text{m}$ . The measured roughness value is very low due to fine polish. The rms roughness for right surface is  $3.89 \mu\text{m}$ .

## Appendix D – Hydraulic fracture propagation regimes

In this section we follow the mathematical treatment of Bungler et al. (2005). They consider a hydraulic fracture driven by a Newtonian fluid inside an infinite elastic medium. The fracture evolves with respect to three time scales which determine separate regimes. The three time scales include large/small fluid lag, large/small effective viscosity, and large/small fluid leak-off. Let's assume the Newtonian fluid flows inside a penny-shaped fracture and the fluid leak-off follows a carter-type rule. Here, the equations are written in terms of the following terms:

$$E' = \frac{E}{(1-\nu^2)} \quad \bar{\mu} = 12\mu \quad K'_{lc} = 4\sqrt{\frac{2}{\pi}} K_{lc} \quad K'_l = 2K_l \quad (\text{D1})$$

with  $E'$  as the plane strain Young's modulus,  $\mu$ ,  $K_{lc}$ , and  $K_l$  ( $K_l = \sqrt{\frac{\Delta p \phi k}{2\mu}}$ ) represent the fluid viscosity, rock fracture

toughness and fluid loss constant, respectively. Now, the solution includes solving for the fracture width  $b$ , fracture radius  $r_f$ , fluid-filled fracture radius  $r_{fw}$ , and the net pressure  $p_n = p - \sigma_c$ . The pressure inside the lag region is solved using the diffusion function which was derived earlier by Detournay and Cheng (1992). The crack opening and pressure are also related using linear elasticity for radial crack system based on Sneddon's solution. Now, the  $r_f$  and  $r_{fw}$  can be found using global conservation of mass and fracture criteria ( $K_I = K_{Ic}$ ), respectively. We define three characteristic dimensionless times:

$$M = \left(\frac{t_m}{t}\right)^{\frac{2}{5}} \quad S = \left(\frac{t}{t_0}\right)^{\frac{1}{5}} \quad C = \left(\frac{t}{t_c}\right)^{\frac{3}{10}} \quad (D2)$$

In which the following equations are used:

$$t_m = \left(\frac{\bar{\mu}^5 q_0^3 E'^{13}}{K'^{18}}\right)^{1/2} \quad t_0 = \frac{K'^6}{\sigma_0^5 q_0 E'} \quad t_c = \left(\frac{K'^4 q_0}{K'_l^5 E'^4}\right)^{2/3} \quad (D3)$$

The three  $M$ ,  $S$ ,  $C$  invariants specify a fracture system. In other words, a fracture system is defined with a unique set of these three time constants.  $M$  represents the viscosity term in these equations.  $S$  is the stress term which governs the fluid lag due to the minimum stress acting against the fracture opening.  $C$  is related to the fluid leak-off into the formation. Depending on the relative time with respect to the time parameters, i.e.  $t_m$ ,  $t_0$ ,  $t_c$ , either of these mechanisms could dominate the process. If we notice again in equations D3, these terms are independent as the terms  $\bar{\mu}$ ,  $\sigma_0$ ,  $K'_l$  appear only in  $t_m$ ,  $t_0$ ,  $t_c$ , respectively. For example if  $t \ll t_m$ , then the viscosity ( $M$ ) dominates the process. At early times the viscosity and fluid lag dominate the process, and leakoff is negligible. Bungler et al. (2005) call this regime as "O". Knowing the experiments in the lab are restricted by finite length, we define this maximum achievable length as  $H$ . According to the equation D2, the relation between the fracture radius and this maximum length now becomes:

$$\frac{L}{H} = \left(\frac{t}{t_h}\right)^{2/5} \quad \text{and} \quad t_h = \frac{H^{5/2} K'}{q_0 E'} \quad (D4)$$

This equation assumes that we are in regime where  $\gamma_f = 0$  (1). The term  $t_h$  gives us the estimated time for each experiment. Now, we define three design parameters as:

$$\psi_1 = \frac{t_m}{t_h} \quad \psi_2 = \frac{t_0}{t_h} \quad \psi_3 = \frac{t_c}{t_h} \quad (D5)$$

Substitution of time parameters result in the following relations:

$$\psi_1 = \left(\frac{\bar{\mu}^5 q_0^5 E'^{15}}{H^5 K'^{20}}\right)^{1/2} \quad \psi_2 = \frac{K'^5}{\sigma_0^5 H^{5/2}} \quad \psi_3 = \left(\frac{K'^{10} q_0^{10}}{K'_l^{20} H^{15} E'^{10}}\right)^{1/6} \quad (D6)$$

The HF experiments in this report were conducted using water with viscosity of 1 cp and an injection rate of 2.6 cc/min. The minimum *in-situ* stress was 5 MPa. Solnhofen has a Young's modulus of 40 GPa and Poisson's ratio of 0.28. The tensile strength and fracture toughness are 16 MPa, and 1.8 MPa.m<sup>0.5</sup>, respectively. The leakoff constant is taken as 2×10<sup>-6</sup> m.s<sup>-0.5</sup>, based on  $K_l = \sqrt{\frac{\Delta p \phi k}{2\mu}}$ . The fracture length in our sample is equal to 18 mm. Based on these values we obtain  $\psi_1 = 3 \times 10^{-7}$ ,  $\psi_2 = 5 \times 10^{-4}$ ,  $\psi_3 = 4 \times 10^3$ . This sets of constants are in the toughness-dominated regime (see Table D1). Here, we only show the parameters for Solnhofen limestone. PMMA experiments are in the same regime. Other sets of three parameters and their relevant fracture regime is summarized in Table D1.

**Table D 1. Dominant fracture regimes for different values of fracture constants (see equation D13 and Bungler et al. (2015)).**

$\psi_3 \gg 1$	$\psi_3 \ll 1$ (leakoff)
----------------	--------------------------

---

	$\psi_1 \ll 1$	$\psi_1 \gg 1$	$\psi_1 \ll 1$	$\psi_1 \gg 1$
$\psi_2 \ll 1$	Toughness	Viscosity	Toughness	Viscosity
$\psi_2 \gg 1$	Toughness	Viscosity and Fluid lag	Toughness	Viscosity and Fluid lag